Structural differences in amyloid-β fibrils from brains of nondemented elderly individuals and Alzheimer's disease patients

Ujjayini Ghosh[a,b], Wai-Ming Yau[a], John Collinge[c,d], and Robert Tycko[a,1]

[a]Laboratory of Chemical Physics, National Institute of Diabetes and Digestive and Kidney Diseases, NIH, Bethesda, MD 20892-0520; [b]Department of Chemistry, Michigan State University, East Lansing, MI 48824; [c]Medical Research Council Prion Unit, University College London, London W1W 7FF, United Kingdom; and [d]Institute of Prion Diseases, University College London, London W1W 7FF, United Kingdom

Edited by Susan Marqusee, University of California, Berkeley, CA, and approved September 20, 2021 (received for review June 27, 2021)

Although amyloid plaques composed of fibrillar amyloid-β (Aβ) assemblies are a diagnostic hallmark of Alzheimer's disease (AD), quantities of amyloid similar to those in AD patients are observed in brain tissue of some nondemented elderly individuals. The relationship between amyloid deposition and neurodegeneration in AD has, therefore, been unclear. Here, we use solid-state NMR to investigate whether molecular structures of Aβ fibrils from brain tissue of nondemented elderly individuals with high amyloid loads differ from structures of Aβ fibrils from AD tissue. Two-dimensional solid-state NMR spectra of isotopically labeled Aβ fibrils, prepared by seeded growth from frontal lobe tissue extracts, are similar in the two cases but with statistically significant differences in intensity distributions of cross-peak signals. Differences in solid-state NMR data are greater for 42-residue amyloid-β (Aβ42) fibrils than for 40-residue amyloid-β (Aβ40) fibrils. These data suggest that similar sets of fibril polymorphs develop in nondemented elderly individuals and AD patients but with different relative populations on average.

amyloid structure | Alzheimer's disease | solid-state NMR

Amyloid plaques in brain tissue, containing fibrils formed by amyloid-β (Aβ) peptides, are one of the diagnostic pathological signatures of Alzheimer's disease (AD). Clear genetic and biomarker evidence indicates that Aβ is key to AD pathogenesis (1). However, Aβ is present as a diverse population of multimeric assemblies, ranging from soluble oligomers to insoluble fibrils and plaques, and may lead to neurodegeneration by a number of possible mechanisms (2–7).

One argument against a direct neurotoxic role for Aβ plaques and fibrils in AD is the fact that plaques are not uncommon in the brains of nondemented elderly people, as shown both by traditional neuropathological studies (8, 9) and by positron emission tomography (10–13). On average, the quantity of amyloid is greater in AD patients (10) and (at least in some studies) increases with decreasing cognitive ability (12, 14, 15) or increasing rate of cognitive decline (16). However, a high amyloid load does not necessarily imply a high degree of neurodegeneration and cognitive impairment (11, 13, 17).

A possible counterargument comes from studies of the molecular structures of Aβ fibrils, which show that Aβ peptides form multiple distinct fibril structures, called fibril polymorphs (18–20). Polymorphism has been demonstrated for fibrils formed by both 40-residue amyloid-β (Aβ40) (19, 21–24) and 42-residue amyloid-β (Aβ42) (22, 25–29) peptides, the two main Aβ isoforms. Among people with similar total amyloid loads, variations in neurodegeneration and cognitive impairment may conceivably arise from variations in the relative populations of different fibril polymorphs. As a hypothetical example, if polymorph A was neurotoxic but polymorph B was not, then people whose Aβ peptides happened to form polymorph A would develop AD, while people whose Aβ peptides happened to form polymorph B would remain cognitively normal. In practice, brains may contain a population of different propagating and/or neurotoxic Aβ species, akin to prion quasispecies or "clouds," and the relative proportions of these and their dynamic interplay may affect clinical phenotype and rates of progression (30).

Well-established connections between molecular structural polymorphism and variations in other neurodegenerative diseases lend credence to the hypothesis that Aβ fibril polymorphism plays a role in variations in the characteristics of AD. Distinct strains of prions causing the transmissible spongiform encephalopathies have been shown to involve different molecular structural states of the mammalian prion protein PrP (30–32). Distinct tauopathies involve different polymorphs of tau protein fibrils (33–37). In the case of synucleopathies, α-synuclein has been shown to be capable of forming polymorphic fibrils (38–40) with distinct biological effects (41–43).

Experimental support for connections between Aβ polymorphism and variations in characteristics of AD comes from polymorph-dependent fibril toxicities in neuronal cell cultures (19), differences in neuropathology induced in transgenic mice by injection of amyloid-containing extracts from different sources (44–46), differences in conformation and stability with respect to chemical denaturation of Aβ assemblies prepared from brain tissue of rapidly or slowly progressing AD patients

Significance

Alzheimer's disease (AD) patients develop amyloid deposits, containing amyloid-β (Aβ) fibrils, in their brain tissue. Although amyloid is a likely contributor to AD dementia, similar amyloid loads occur in some nondemented elderly individuals. Molecular structures of Aβ fibrils are known to be variable. We, therefore, investigate whether structures of Aβ fibrils derived from cerebral cortical tissue of nondemented elderly subjects differ from structures from AD patients. We find statistically significant, but subtle, differences between NMR spectra of Aβ fibrils from nondemented elderly subjects and analogous spectra of fibrils from AD patients. Thus, similar structures develop but with different relative populations on average. Other factors may be primary determinants of cognitive status in individuals with high amyloid loads.

Author contributions: U.G., J.C., and R.T. designed research; U.G. and R.T. performed research; W.-M.Y. contributed new reagents/analytic tools; U.G. and R.T. analyzed data; and U.G., W.-M.Y., J.C., and R.T. wrote the paper.

The authors declare no competing interest.

This article is a PNAS Direct Submission.

[1]To whom correspondence may be addressed. Email: robertty@mail.nih.gov.

This article contains supporting information online at http://www.pnas.org/lookup/suppl/doi:10.1073/pnas.2111863118/-/DCSupplemental.

Published November 1, 2021.

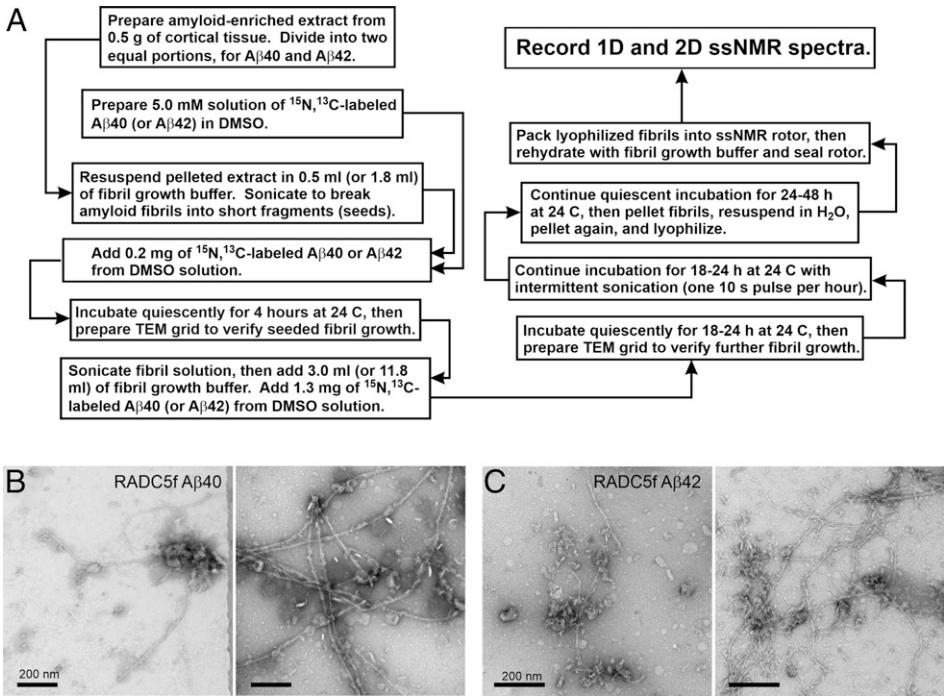

Fig. 1. Preparation of brain-seeded Aβ fibrils for solid-state NMR (ssNMR). (*A*) Flowchart representation of the protocol for preparation of isotopically labeled Aβ40 and Aβ42 fibril samples by seeded growth from amyloid in human brain extract. (*B*) TEM images of negatively stained Aβ40 fibrils prepared from frontal lobe tissue of RADC subject 5. Images are shown after the initial 4-h incubation step (*Left*) and after the subsequent 18- to 24-h incubation step (*Right*). (*C*) Same as in *A* but for Aβ42 fibrils. (Scale bars: 200 nm.)

(47), and differences in fluorescence emission spectra of structure-sensitive dyes bound to amyloid plaques in tissue from sporadic or familial AD patients (48, 49).

Solid-state NMR spectroscopy is a powerful method for investigating fibril polymorphism because even small, localized changes in molecular conformation or structural environment produce measurable changes in ^{13}C and ^{15}N NMR chemical shifts (i.e., in NMR frequencies of individual carbon and nitrogen sites). Full molecular structural models for amyloid fibrils can be developed from large sets of measurements on structurally homogeneous samples (21, 25, 26, 29, 38, 50). Alternatively, simple two-dimensional (2D) solid-state NMR spectra can serve as structural fingerprints, allowing assessments of polymorphism and comparisons between samples from different sources (22, 51).

Solid-state NMR requires isotopic labeling and milligram-scale quantities of fibrils, ruling out direct measurements on amyloid fibrils extracted from brain tissue. However, Aβ fibril structures from autopsied brain tissue can be amplified and isotopically labeled by seeded fibril growth, in which fibril fragments (i.e., seeds) in a brain tissue extract are added to a solution of isotopically labeled peptide (21, 22, 52). Labeled "daughter" fibrils that grow from the seeds retain the molecular structures of the "parent" fibrils, as demonstrated for Aβ (19, 21, 24, 53) and other (54, 55) amyloid fibrils. Solid-state NMR measurements on the brain-seeded fibrils then provide information about molecular structures of fibrils that were present in the brain tissue at the time of autopsy. Using this approach, Lu et al. (21) developed a full molecular structure for Aβ40 fibrils derived from one AD patient with an atypical clinical history (patient 1), showed that Aβ40 fibrils from a second patient with a typical AD history (patient 2) were qualitatively different in structure, and showed that the predominant brain-derived Aβ40 polymorph was the same in multiple regions of the cerebral cortex from each patient. Subsequently, Qiang et al. (22) prepared isotopically labeled Aβ40 and Aβ42 fibrils from frontal, occipital, and parietal lobe tissue of 15 patients in three categories, namely typical long-duration Alzheimer's disease (t-AD), the posterior cortical atrophy variant of Alzheimer's disease (PCA-AD), and rapidly progressing Alzheimer's disease (r-AD). Quantitative analyses of 2D solid-state NMR spectra led to the conclusions that Aβ40 fibrils derived from t-AD and PCA-AD tissue were indistinguishable, with both showing the same predominant polymorph; that Aβ40 fibrils derived from r-AD tissue were more structurally heterogeneous (i.e., more polymorphic); and that Aβ42 fibrils derived from all three categories were structurally heterogeneous, with at least two prevalent Aβ42 polymorphs (22).

In this paper, we address the question of whether Aβ fibrils that develop in cortical tissue of nondemented elderly individuals with high amyloid loads are structurally distinguishable from fibrils that develop in cortical tissue of AD patients. As described below, quantitative analyses of 2D solid-state NMR spectra of brain-seeded samples indicate statistically significant differences for both Aβ40 and Aβ42 fibrils. Differences in the 2D spectra are subtle, however, indicating that nondemented individuals and AD patients do not develop entirely different Aβ fibril structures. Instead, data and analyses described below suggest overlapping distributions of fibril polymorphs, with different relative populations on average.

Results

Preparation of Aβ Fibrils. Aβ40 and Aβ42 fibrils were prepared by seeded growth using an amyloid-containing extract from human frontal lobe tissue as the source of seeds. As in the experiments of Qiang et al. (22), Aβ40 was ^{15}N,^{13}C labeled at F19, V24, G25, S26, A30, I31, L34, and M35, and Aβ42 was ^{15}N,^{13}C labeled at F19, G25, A30, I31, L34, and M35. Tissue samples were obtained from the Religious Orders Study of the Rush Alzheimer's Disease Center (RADC) (56). Eight samples were selected from subjects assessed as lacking cognitive

impairment but with high cortical Aβ levels measured by immunohistochemistry (*SI Appendix*, *SI Methods* and Table S1). Ages at death ranged from 85 to 100 y.

Extracts were prepared as described previously (21, 22). Fibrils were then grown with the protocol depicted in Fig. 1*A*. This protocol is identical to the one used by Qiang et al. (22), except that isotopically labeled Aβ, solubilized in dimethyl sulfoxide (DMSO), was added to the sonicated suspension of tissue extract in two steps rather than in a single step (*SI Appendix*, *SI Methods*). This modification of the seeded growth protocol was necessary because tissue samples from RADC were only 0.5 to 0.6 g, whereas tissue samples in the experiments of Qiang et al. (22) were ∼2.0 to 3.0 g. By adding Aβ in two steps, the ratio of DMSO-solubilized Aβ to extract at the beginning of fibril growth was kept approximately constant. To minimize the likelihood of preferential amplification of specific polymorphs (57), sonication conditions that fragment all polymorphs were used, multiple rounds of seeded growth were avoided, and the ratio of Aβ in seeds to soluble Aβ in the second step was large (2:13 ratio).

Fibril samples derived from RADC tissue are denoted RADCnf, with n = 1, 2, … 8 and with "f" indicating frontal lobe tissue. Fig. 1 *B* and *C* shows examples of transmission electron microscope (TEM) images of Aβ40 and Aβ42 fibrils after the initial 4-h growth period and after the subsequent 18- to 24-h period. Full sets of TEM images are shown in *SI Appendix*, Figs. S1 and S2. The TEM images at 4 h show fibrils in all cases, whereas previously reported control experiments with extracts from human cortical tissue that was devoid of Aβ plaques resulted in no detectable fibrils after 4 h (21, 22). The morphologies of Aβ40 and Aβ42 fibrils in the TEM images could not be assessed reliably because, in many cases, extraneous material from the tissue extracts adhered to or partially obscured the fibrils. It should be noted that our tissue extracts are heterogeneous materials, with amyloid representing only a small fraction of the total mass.

Solid-State NMR Spectroscopy of Aβ40 Fibrils. Fig. 2 *A* and *B* shows examples of 2D ^{13}C-^{13}C solid-state NMR spectra of Aβ40 fibrils prepared by seeded growth from RADC tissue extracts. The 2D spectrum in Fig. 2*A* exhibits a single set of relatively sharp and strong cross-peaks, with little intensity in additional signals. This spectrum, therefore, suggests a single predominant Aβ40 fibril polymorph in the RADC1f sample. Additional signals in Fig. 2*B*, indicated by cyan arrows, suggest the presence of at least one additional polymorph with a substantial population in the RADC4f sample. One-dimensional (1D) spectra of all eight RADC Aβ40 samples (*SI Appendix*, Fig. S3 *A* and *C*) show variations in the relative intensities and shapes of the ^{13}C solid-state NMR lines, suggesting variations in polymorph populations. The full set of 2D ^{13}C-^{13}C spectra is shown in *SI Appendix*, Fig. S4.

For comparison, Fig. 2 *C* and *D* shows 2D ^{13}C-^{13}C solid-state NMR spectra of Aβ40 fibrils prepared by seeded growth from one of the t-AD tissue extracts examined by Qiang et al. (22) (sample t-AD4f) and Aβ40 fibrils prepared in vitro without seeding. Spectra in Fig. 2 *B* and *C* are similar to one another, whereas the spectrum in Fig. 2*D* shows broader cross-peaks and additional signals, indicating greater structural heterogeneity in the final fibril sample when fibril growth is initiated by spontaneous nucleation, rather than by seeding.

Fig. 2 *E*–*H* shows 2D ^{15}N-^{13}C solid-state NMR spectra of the same Aβ40 fibrils as in Fig. 2 *A*–*D*. Again, the spectrum of the RADC4f sample (Fig. 2*F*) shows additional cross-peak signals that are not detectable in the spectrum of the RADC1f sample (Fig. 2*E*). The spectrum of the t-AD4f sample (Fig. 2*G*) is similar to that of the RADC4f sample, but differences are more readily apparent than in the 2D ^{13}C-^{13}C spectra. The 2D ^{15}N-^{13}C spectrum of the unseeded sample (Fig. 2*H*) obviously contains many cross-peak signals that are not present in spectra of the other three samples. The 2D ^{15}N-^{13}C spectra of all eight RADC Aβ40 samples are shown in *SI Appendix*, Fig. S5.

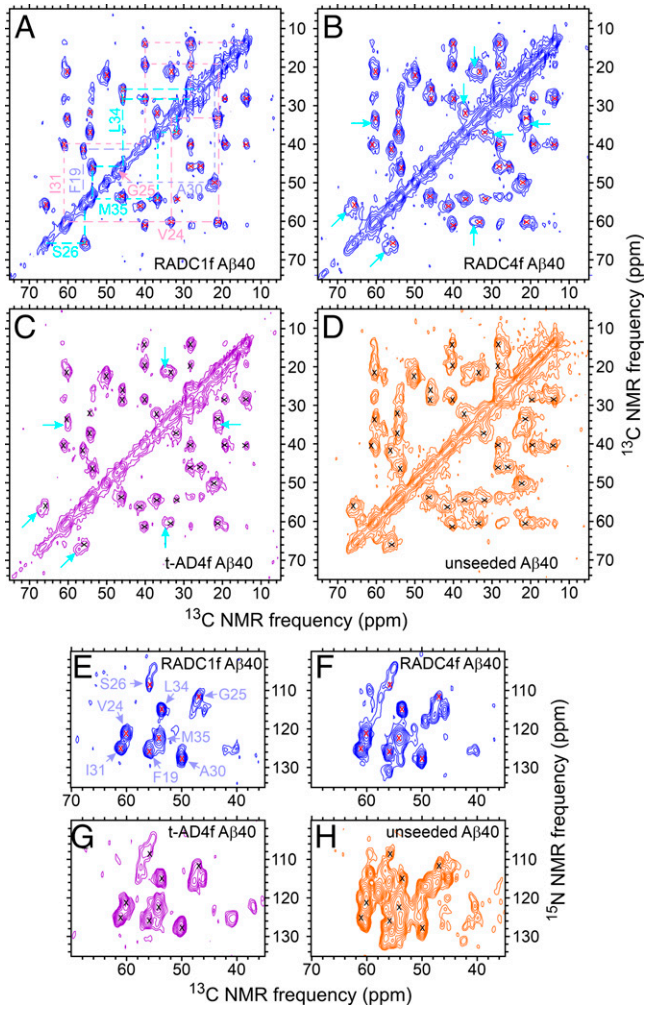

Fig. 2. The 2D solid-state NMR spectra of brain-seeded Aβ40 fibrils with uniform ^{15}N,^{13}C-labeling of F19, V24, G25, S26, A30, I31, L34, and M35. (*A*–*D*) The 2D ^{13}C-^{13}C spectra of fibrils prepared from frontal lobe tissue of RADC subjects 1 and 4, fibrils prepared from frontal lobe tissue of AD patient t-AD4 [as reported previously by Qiang et al. (22)], and unseeded fibrils. Assignments of cross-peak signals to the labeled residues are indicated by cyan, pink, and pastel blue labels and dashed lines in *A*. Red and black X's in *B*–*D* indicate positions of cross-peak signals in *A*. Cyan arrows indicate additional cross-peak signals. Contour levels increase by successive factors of 2.0, with the lowest contour at ∼3.0 times the rms noise level in each spectrum. (*E*–*H*) The 2D ^{15}N-^{13}C spectra of the same fibrils, with similar annotations. Contour levels increase by successive factors of 1.5, with the lowest contour at ∼3.0 times the rms noise level. The full set of 2D spectra of Aβ40 fibrils prepared from RADC samples is given in *SI Appendix*, Figs. S4 and S5.

Solid-State NMR Spectroscopy of Aβ42 Fibrils. Fig. 3 shows 2D ^{13}C-^{13}C and ^{15}N-^{13}C solid-state NMR spectra of RADC3f and RADC7f Aβ42 fibrils, t-AD1f Aβ42 fibrils from the work of Qiang et al. (22), and unseeded Aβ42 fibrils. The 2D spectra of all eight RADC Aβ42 fibrils are shown in *SI Appendix*, Figs. S6 and S7. Both types of 2D spectra show clear differences between the RADC3f and RADC7f samples, suggesting that the main Aβ42 fibril polymorphs in these two samples are different. The 2D spectra of t-AD1f Aβ42 fibrils are also different

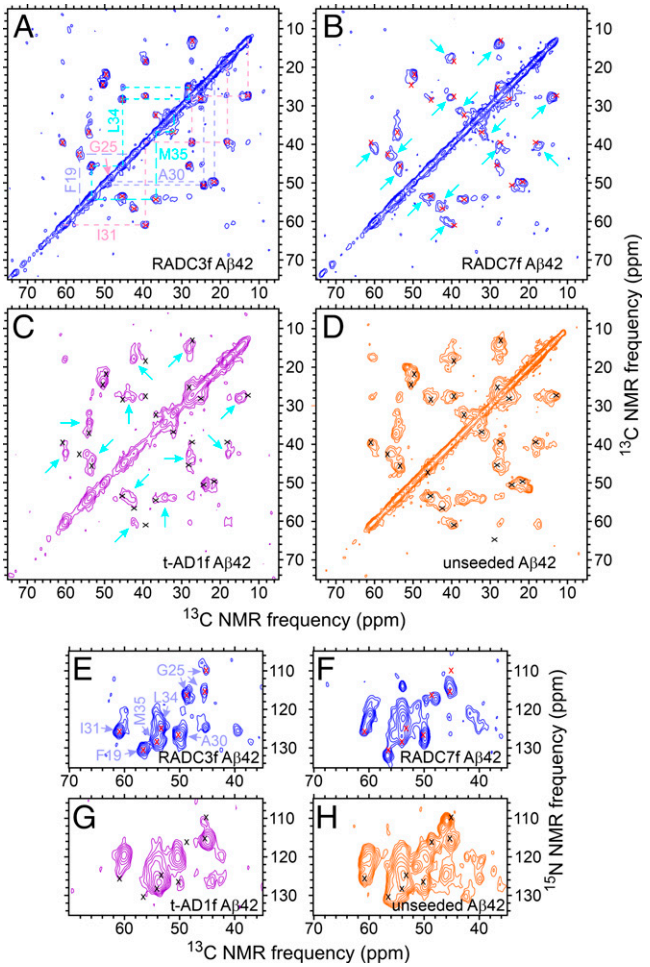

Fig. 3. The 2D solid-state NMR spectra of brain-seeded Aβ42 fibrils with uniform ^{15}N,^{13}C-labeling of F19, G25, A30, I31, L34, and M35. (*A–D*) The 2D ^{13}C-^{13}C spectra of fibrils prepared from frontal lobe tissue of RADC subjects 3 and 7, fibrils prepared from frontal lobe tissue of AD patient t-AD1 [as reported previously by Qiang et al. (22)], and unseeded fibrils. Assignments of cross-peak signals to the labeled residues are indicated by cyan, pink, and pastel blue labels and dashed lines in *A*. Red and black X's in *B–D* indicate positions of cross-peak signals in *A*. Cyan arrows indicate additional cross-peak signals. Contour levels increase by successive factors of 2.0, with the lowest contour at ~3.0 times the rms noise level in each spectrum. (*E–H*) The 2D ^{15}N-^{13}C spectra of the same fibrils, with similar annotations. Contour levels increase by successive factors of 1.5, with the lowest contour at ~3.0 times the rms noise level. The full set of 2D spectra of Aβ42 fibrils prepared from RADC samples is given in *SI Appendix*, Figs. S6 and S7.

from the two RADC samples. The 2D spectra of the unseeded Aβ42 fibrils contain broader cross-peaks and additional cross-peaks, indicating greater structural heterogeneity.

As with the Aβ40 fibrils, 1D spectra of all eight RADC Aβ42 samples (*SI Appendix*, Fig. S3 *B* and *D*) show variations in the relative intensities and shapes of the ^{13}C solid-state NMR lines. These spectra also show large variations in total signal amplitude (e.g., a factor of four difference between RADC4f and RADC8f Aβ42 samples) (*SI Appendix*, Fig. S3*D*), although the amount of isotopically labeled Aβ42 used in the seeded fibril growth protocol was the same for each sample. Variations in signal amplitude are attributable to variations in the quantities of seed-competent Aβ42 amyloid in the tissue samples. In particular, signals from the RADC2f Aβ42 sample were very weak, leading to barely detectable cross-peaks in 2D spectra of this sample (*SI Appendix*, Figs. S6 and S7).

rmsd Analyses. If the brain-seeded Aβ40 and Aβ42 fibril samples contained only a small number of polymorphs and if their cross-peak signals were well resolved in the 2D spectra, then it would be possible to estimate the populations of individual polymorphs in each sample from cross-peak volumes in the 2D spectra. In reality, however, the 2D spectra contain complicated cross-peak patterns, with contributions from multiple polymorphs that are not well resolved. Therefore, we used two objective methods for quantitatively analyzing and comparing 2D spectra that do not require assignment of cross-peaks to individual polymorphs (58).

In the first method, we calculated pairwise root-mean-squared deviations (rmsds) among signal amplitudes in the 2D spectra after identifying regions of the spectra that contain signals above the noise level, normalizing the total signal amplitudes, and optimizing the relative scaling of signal amplitudes (*SI Appendix*, *SI Methods*). Fig. 4 displays pairwise rmsds among 2D solid-state NMR spectra of Aβ40 and Aβ42 fibrils as heat maps, with small rmsd values in blue, intermediate values in white and yellow, and large values in red. The 2D spectra of the eight RADC-seeded samples are included (59), along with 2D spectra of t-AD and PCA-AD samples reported previously by Qiang et al. (22, 60). [The 2D spectra of all t-AD and PCA-AD samples appear in extended data figures 2 and 3 of the paper by Qiang et al. (22) and are available at https://data.mendeley.com/datasets/tbp45pm92x/1.] Fibrils derived by seeded growth from amyloid-containing extracts of t-AD and PCA-AD tissue samples are denoted by t-ADnx and PCAnx, where n is the patient number and x is "f," "o," or "p" for frontal, occipital, or parietal lobe tissue, respectively. Although rmsd values vary considerably when spectra within or between each of the three tissue categories (i.e., RADC, t-AD, and PCA-AD) are compared, the overall color patterns in Fig. 4 suggest that 2D spectra of RADC samples are more similar to one another (i.e., have smaller pairwise rmsds on average) than to 2D spectra of t-AD or PCA-AD samples. Moreover, as shown previously by Qiang et al. (22), t-AD and PCA-AD samples appear to be indistinguishable. The sensitivity of rmsd values to differences among 2D spectra is evident, for example, from the observation that 2D ^{13}C-^{13}C spectra of RADC1f and t-AD4f fibrils appear similar in the contour plots in Fig. 2 but have rmsd = 0.28, while 2D ^{13}C-^{13}C spectra of RADC6f and RADC7f are more nearly identical in *SI Appendix*, Fig. S4 and have rmsd = 0.08.

Three statistical tests were used to evaluate the significance of the apparent differences in rmsd values. Results are summarized in Table 1. The 2D spectra of RADC2f Aβ42 were not included in these tests, due to their low signal-to-noise ratios.

First, the two-sample Kolmogorov–Smirnov (KS) test was used to determine whether distributions of rmsd values for pairs of spectra of RADC samples were significantly different from distributions of rmsd values between spectra of RADC samples and spectra of t-AD samples, PCA-AD samples, and combined t-AD and PCA-AD samples. Significant differences (i.e., D statistic greater than critical value, with significance parameter $\alpha = 0.05$) were found in nearly all cases for both Aβ40 and Aβ42 fibrils and for both 2D ^{13}C-^{13}C spectra and 2D ^{15}N-^{13}C spectra. The only exceptions were when rmsds between 2D spectra of pairs of RADC Aβ42 samples were compared with rmsds between spectra of RADC Aβ42 samples and spectra of PCA-AD Aβ42 samples. The absence of statistical significance in these cases may be due to the small number of PCA-AD Aβ42 samples for which 2D spectra were available.

Next, the two-tail, two-sample Wilcoxon–Mann–Whitney (WMW) test was used to confirm the KS results. The WMW test indicated significant differences between distributions of rmsd values ($P \leq 0.002$) in all cases where differences were significant according to the KS test.

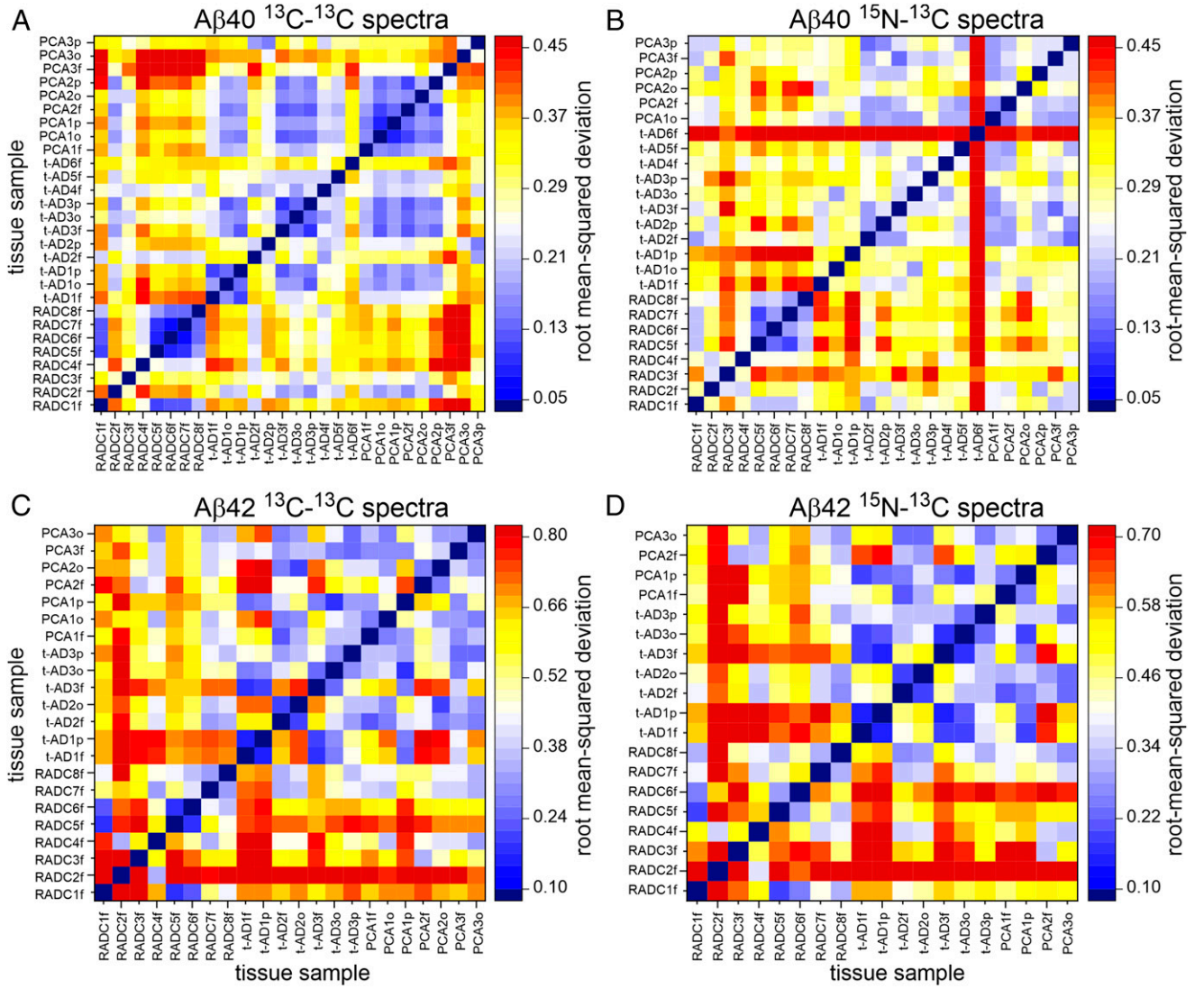

Fig. 4. Comparisons of 2D solid-state NMR spectra of isotopically labeled Aβ40 and Aβ42 fibrils derived from cortical tissue of nondemented subjects (RADCnf, where n is the patient number), typical AD patients (t-ADnx, where x is f, o, or p for frontal, occipital, or parietal lobe tissue, respectively), and posterior cortical atrophy patients (PCAnx). Color scales represent rmsds between cross-peak signal amplitudes in pairs of 2D spectra after normalization and optimal scaling of the 2D spectra as described in the text. (*A* and *B*) rmsd heat maps for 2D ^{13}C-^{13}C and ^{15}N-^{13}C spectra of Aβ40 fibrils. (*C* and *D*) rmsd heat maps for 2D ^{13}C-^{13}C and ^{15}N-^{13}C spectra of Aβ42 fibrils.

Finally, Welch's *t* test (WTT) was used to determine the statistical significance of differences between the average rmsd value for pairs of spectra of RADC samples and the average rmsd value between spectra of RADC samples and spectra of t-AD samples, PCA-AD samples, and combined t-AD and PCA-AD samples. Again, differences were found to be significant ($P \leq 0.002$) in all cases except when rmsds between 2D spectra of pairs of RADC Aβ42 samples were compared with rmsds between spectra of RADC Aβ42 samples and spectra of PCA-AD Aβ42 samples.

In addition to the unseeded in vitro fibrils whose spectra are shown in Figs. 2 *D* and *H* and 3 *D* and *H*, Aβ40 and Aβ42 fibrils were grown in the presence of extract from occipital lobe tissue that was devoid of detectable amyloid (22). *SI Appendix*, Fig. S8 shows 2D spectra of these fibrils, along with their rmsds relative to the 2D spectra of RADC, t-AD, and PCA-AD fibril samples. In most cases, rmsd values in *SI Appendix*, Fig. S8 are greater than the values in Table 1. Thus, we have no evidence that nonamyloid components of cortical tissue extracts promote the formation of the specific fibril polymorphs that we observe in fibrils created by seeding with amyloid-containing extracts.

Principal Component Analyses. As a second method of assessing similarities and differences among samples, we used principal component analysis (49, 61, 62). As applied to 2D solid-state NMR spectra (22), principal component analysis is a mathematical procedure for representing each experimental 2D spectrum $E_k(\nu_1,\nu_2)$ as a linear combination of principal component spectra $P_q(\nu_1,\nu_2)$, with principal values η_q and coefficients c_{kq} [i.e., $E_k(\nu_1,\nu_2) = \sum_{q=1}^{N} c_{kq}\eta_q P_q(\nu_1,\nu_2)$, where N is the number of experimental 2D spectra and ν_1 and ν_2 are the two frequency axes of the 2D spectra]. Principal values are nonnegative, and principal component spectra are ordered by decreasing principal value (i.e., $\eta_q \geq \eta_{q'}$ if $q < q'$). The first principal component $P_1(\nu_1,\nu_2)$ is an approximate average of the experimental 2D spectra. Subsequent principal components represent variations among the experimental 2D spectra with decreasing importance.

Table 1. Statistics for rmsd analyses

Data type	Comparison 1	rmsd 1	Comparison 2	rmsd 2	KS D statistic	KS critical value	WMW U statistic	WMW P value	WTT ν	WTT t statistic	WTT P value
2D ^{13}C-^{13}C Aβ40	RADC vs. RADC (n = 56)	0.246 (0.104)	RADC vs. t-AD (n = 176)	0.311 (0.065)	0.312*	0.222*	3,224.5*	<0.001*	69.10*	–4.322*	<0.001*
2D ^{13}C-^{13}C Aβ40	RADC vs. RADC (n = 56)	0.246 (0.104)	RADC vs. PCA-AD (n = 144)	0.359 (0.104)	0.456*	0.228*	1,811.5*	<0.001*	90.19*	–7.032*	<0.001*
2D ^{13}C-^{13}C Aβ40	RADC vs. RADC (n = 56)	0.246 (0.104)	RADC vs. t-AD + PCA-AD (n = 320)	0.332 (0.082)	0.357*	0.210*	5,036*	<0.001*	67.34*	–5.827*	<0.001*
2D ^{15}N-^{13}C Aβ40	RADC vs. RADC (n = 56)	0.263 (0.079)	RADC vs. t-AD (n = 176)	0.354 (0.088)	0.537*	0.222*	2,113*	<0.001*	101.17*	–7.197*	<0.001*
2D ^{15}N-^{13}C Aβ40	RADC vs. RADC (n = 56)	0.263 (0.079)	RADC vs. PCA-AD (n = 96)	0.302 (0.079)	0.359*	0.243*	1,748*	<0.001*	90.08*	–3.133*	0.002*
2D ^{15}N-^{13}C Aβ40	RADC vs. RADC (n = 56)	0.263 (0.079)	RADC vs. t-AD + PCA-AD (n = 272)	0.336 (0.083)	0.473*	0.213*	3,861*	<0.001*	81.24*	–6.112*	<0.001*
2D ^{13}C-^{13}C Aβ42	RADC vs. RADC (n = 42)	0.378 (0.196)	RADC vs. t-AD (n = 98)	0.549 (0.146)	0.388*	0.266*	1,235.5*	<0.001*	59.39*	–3.792*	<0.001*
2D ^{13}C-^{13}C Aβ42	RADC vs. RADC (n = 42)	0.378 (0.196)	RADC vs. PCA-AD (n = 98)	0.483 (0.123)	0.218†	0.266†	1,731†	0.137†	58.63†	–1.50†	0.139†
2D ^{13}C-^{13}C Aβ42	RADC vs. RADC (n = 42)	0.378 (0.196)	RADC vs. t-AD + PCA-AD (n = 196)	0.516 (0.147)	0.260*	0.246*	2,966.5*	0.004*	50.67*	–2.761*	0.008*
2D ^{15}N-^{13}C Aβ42	RADC vs. RADC (n = 42)	0.339 (0.159)	RADC vs. t-AD (n = 98)	0.487 (0.147)	0.340*	0.266*	1,248.5*	<0.001*	75.41*	–3.888*	<0.001*
2D ^{15}N-^{13}C Aβ42	RADC vs. RADC (n = 42)	0.339 (0.159)	RADC vs. PCA-AD (n = 56)	0.435 (0.126)	0.202†	0.294†	981†	0.162†	84.79†	–1.558†	0.122†
2D ^{15}N-^{13}C Aβ42	RADC vs. RADC (n = 42)	0.339 (0.159)	RADC vs. t-AD + PCA-AD (n = 154)	0.468 (0.146)	0.260*	0.252*	2,229.5*	0.002*	63.65*	–3.262*	0.002*

KS tests used $\alpha = 0.05$. WMW P values are two-tail values. The WTT degree of freedom is ν. rmsd 1 and rmsd 2 values are mean values, with SDs in parentheses. The KS and WMW tests evaluate whether distributions of rmsd values from comparisons 1 and 2 are significantly different. The WTT test evaluates whether the mean rmsd values are significantly different.

*Statistically significant differences between rmsd values for comparison 1 and rmsd values for comparison 2.

†An absence of statistical significance.

Principal component analyses were carried out as described in *SI Appendix*, *SI Methods*, including spectra of RADC, t-AD, and PCA-AD samples. The total number of 2D spectra was n = 28 for 2D ^{13}C-^{13}C spectra of Aβ40 fibrils, n = 25 for 2D ^{15}N-^{13}C spectra of Aβ40 fibrils, n = 22 for 2D ^{13}C-^{13}C spectra of Aβ42 fibrils, and n = 19 for 2D ^{15}N-^{13}C spectra of Aβ42 fibrils. The first three principal component spectra for each set of 2D spectra are plotted in *SI Appendix*, Figs. S9 and S10. Principal values are plotted in *SI Appendix*, Fig. S11.

Values of the coefficients c_{k1}, c_{k2}, and c_{k3} from principal component analyses of the four sets of 2D spectra are plotted in Fig. 5. As expected, average values of c_{k1} are nearly equal for RADC, t-AD, and PCA-AD samples. Average values of c_{k2} and c_{k3} vary, suggesting differences among 2D spectra from the three tissue categories. As for the rmsd analyses, three statistical tests were used to evaluate significance. Results are summarized in Table 2.

The KS test indicates that the distribution of c_{2k} values for 2D ^{13}C-^{13}C spectra of RADC Aβ40 fibrils differs significantly ($\alpha = 0.5$) from distributions of c_{2k} values for 2D ^{13}C-^{13}C spectra of t-AD Aβ40 fibrils, PCA-AD Aβ40 fibrils, and combined t-AD and PCA-AD Aβ40 fibrils. The same is true for 2D ^{13}C-^{13}C spectra of Aβ42 fibrils. The KS test also indicates significant differences between the distribution of c_{2k} values for 2D ^{15}N-^{13}C spectra of RADC Aβ42 fibrils and distributions of c_{2k} values for 2D ^{15}N-^{13}C spectra of t-AD Aβ42 fibrils and combined t-AD and PCA-AD Aβ42 fibrils, as well as significant differences between the distribution of c_{1k} values for 2D ^{13}C-^{13}C spectra of RADC Aβ42 fibrils and distributions of c_{1k} values for 2D ^{13}C-^{13}C spectra of t-AD Aβ42 fibrils and combined t-AD and PCA-AD Aβ42 fibrils.

The WMW test indicates significant differences ($P \leq 0.005$) in all cases where differences were significant according to the KS test. Additionally, the WMW test indicates significant differences ($P \leq 0.029$) between the distribution of c_{2k} values for 2D ^{15}N-^{13}C spectra of RADC Aβ40 fibrils and distributions of c_{2k} values for 2D ^{15}N-^{13}C spectra of t-AD Aβ40 fibrils and combined t-AD and PCA-AD Aβ42 fibrils, as well as a significant difference ($P = 0.034$) between the distribution of c_{1k} values for 2D ^{13}C-^{13}C spectra of RADC Aβ42 fibrils and the distribution of c_{1k} values for 2D ^{13}C-^{13}C spectra of PCA-AD Aβ42 fibrils.

Finally, for both Aβ40 and Aβ42 fibrils and for both 2D ^{13}C-^{13}C spectra and 2D ^{15}N-^{13}C spectra, WTT indicates significant differences ($P \leq 0.029$) between average values of c_{2k} for RADC samples and average values of c_{2k} for t-AD samples, PCA-AD samples, and combined t-AD and PCA-AD samples, except when 2D ^{15}N-^{13}C spectra of RADC Aβ42 samples are compared with 2D ^{15}N-^{13}C spectra of PCA-AD Aβ42 samples. WTT also indicates significant differences ($P \leq 0.040$) between the average value of c_{1k} for 2D ^{13}C-^{13}C spectra of RADC Aβ42 fibrils and the average values of c_{1k} for 2D ^{13}C-^{13}C spectra of t-AD Aβ42 fibrils, PCA-AD Aβ42 fibrils, and combined t-AD and PCA-AD Aβ42 fibrils.

Discussion

How Do Aβ Fibrils from Nondemented Subjects Differ from Aβ Fibrils from AD Patients? As described above, we have prepared isotopically labeled Aβ40 and Aβ42 fibrils by seeded growth

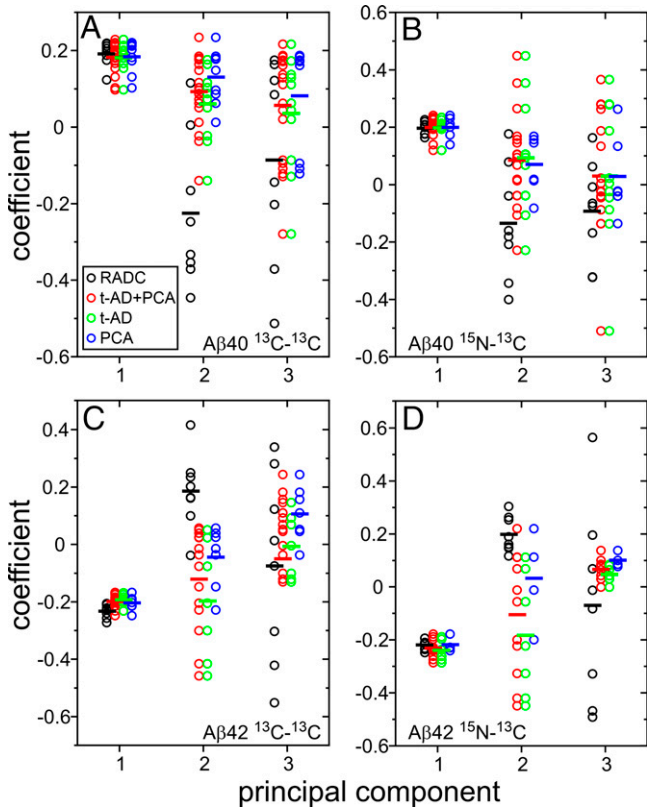

Fig. 5. Comparisons of 2D solid-state NMR spectra of isotopically labeled Aβ40 and Aβ42 fibrils by principal component analysis. (*A*) Coefficients of the first three principal components in 2D ^{13}C-^{13}C spectra of Aβ40 fibrils derived from RADC, t-AD, and PCA-AD tissue samples. Color-coded circles indicate coefficients for individual 2D spectra. Bars indicate average values. Combined data for t-AD and PCA-AD samples are shown as "t-AD + PCA." (*B*) Same as in *A* for 2D ^{15}N-^{13}C spectra. (*C* and *D*) Same as in *A* and *B* but for Aβ42 fibrils.

from amyloid-containing extracts of cortical tissue from nondemented subjects with high amyloid loads (RADC samples), carried out solid-state NMR measurements on these fibrils, and compared the resulting 2D solid-state NMR spectra with previously reported (22) 2D spectra of isotopically labeled Aβ40 and Aβ42 fibrils derived from cortical tissue of AD patients (t-AD and PCA-AD samples). Both rmsd and principal component analyses indicate statistically significant differences between spectra from RADC samples and spectra from t-AD and PCA-AD samples.

However, the differences are subtle. The 2D spectra are variable, both for fibrils derived from tissue of nondemented subjects (Figs. 2 and 3 and *SI Appendix*, Figs. S4–S7) and for fibrils derived from tissue of AD patients (22). For example, 2D spectra of RADC1f Aβ40 fibrils show a single set of strong cross-peak signals, indicating a single predominant structure and minimal polymorphism, while spectra of RADC3f Aβ40 fibrils show multiple sets of signals, indicating a greater degree of polymorphism. Roughly speaking, 2D spectra of other RADC Aβ40 fibrils are intermediate between those of RADC1f and RADC3f.

As a means of visualizing the differences between typical 2D spectra of fibrils derived from the three tissue categories, we constructed 2D spectra from the first three principal components (*SI Appendix*, Figs. S9 and S10) using the average values of c_{1k}, c_{2k}, and c_{3k} for each category. The resulting "average 2D spectra" are shown in Figs. 6 and 7. For Aβ40 fibrils (Fig. 6), average 2D ^{13}C-^{13}C and ^{15}N-^{13}C spectra of RADC samples are similar to the corresponding average spectra of t-AD and PCA-AD spectra (which are essentially indistinguishable from one another). Differences in the relative intensities of cross-peak components arising from F19, V24, G25, and S26 are indicated by magenta arrows. For S26 and V24, the positions of maximal cross-peak intensity are shifted in the average 2D ^{13}C-^{13}C spectra of t-AD and PCA-AD samples, relative to the positions of maximal cross-peak intensity in the average 2D ^{13}C-^{13}C spectra of RADC samples.

For Aβ42 (Fig. 7), differences between average 2D spectra of RADC samples and average 2D spectra of t-AD and PCA-AD samples are more pronounced. The most obvious differences are in the relative intensities of cross-peak components arising from F19, G25, A30, and I31. For G25, A30, and I31, positions of maximal cross-peak intensity are shifted in average 2D ^{13}C-^{13}C or ^{15}N-^{13}C spectra of t-AD and PCA-AD samples, relative to corresponding positions of maximal cross-peak intensity in average 2D spectra of RADC samples.

Thus, from the average 2D spectra, it appears that both nondemented subjects and AD patients develop distributions of Aβ40 and Aβ42 polymorphs in their cortical tissue. The distributions for nondemented subjects and AD patients overlap but exhibit statistically significant differences. The most obvious differences in the average 2D spectra are in cross-peak signals arising from G25, A30, and I31 in brain-seeded Aβ42 fibrils. Other isotopically labeled residues in both Aβ40 and Aβ42 fibrils also exhibit significant differences in their average cross-peak intensity distributions.

Aβ40 vs. Aβ42. Our finding of greater differences on average for Aβ42 fibrils suggests that the distribution of Aβ42 fibril polymorphs in cortical tissue may be more predictive of cognitive impairment than the distribution of Aβ40 fibril polymorphs. It should be recognized that cross-seeding between different Aβ isoforms, as observed in vitro under certain circumstances (63), may affect this finding. If cross-seeding is significant, solid-state NMR data for Aβ42 may not reflect only the properties of Aβ42 fibrils in the original tissue. Nonetheless, it seems unlikely that seeding of Aβ42 by Aβ40 fibrils in our tissue extracts would produce greater structural variations among brain-seeded Aβ42 fibrils than among brain-seeded Aβ40 fibrils. Moreover, even if the molecular structures and structural distributions of brain-seeded fibrils in our experiments do not precisely match those of fibrils in the original cortical tissue, the fact that we see differences in solid-state NMR spectra of fibrils derived from different groups of tissue samples supports the existence of structural differences in the original fibrils.

Implications for the Role of Aβ Fibril Polymorphism in AD. Work described above was motivated by the goal of determining whether Aβ fibrils that develop in brain tissue of nondemented elderly subjects are structurally distinct from those that develop in brain tissue of AD patients. If clear differences in fibril structure exist, it would provide a potential explanation for the observation of high amyloid loads in some elderly individuals who are cognitively normal according to standard assessments (11, 13, 17). Our finding that 2D solid-state NMR spectra of fibrils derived from cortical tissue of nondemented elderly individuals exhibit statistically significant differences from, but are nonetheless similar to, spectra of fibrils derived from cortical tissue of AD patients is best explained by the occurrence of the same or similar sets of fibril polymorphs in both cases but with differences in the relative populations of these polymorphs on average. It is conceivable that certain polymorphs with enhanced populations in AD patients contribute most strongly to neurodegeneration. On the other hand, our data certainly do not rule out the possibility that factors other than Aβ fibril

Table 2. Statistics for principal component analyses

Data type	Principal component	Tissue category	*n*	Average coefficient	KS *D* statistic	KS critical value	WMW *U* statistic	WMW *P* value	WTT *ν*	WTT *t* statistic	WTT *P* value
2D ^{13}C-^{13}C Aβ40	1	RADC	8	0.192 (0.031)							
2D ^{13}C-^{13}C Aβ40	1	t-AD	11	0.182 (0.035)	0.318†	0.637†	53†	0.467†	16.09†	0.623†	0.542†
2D ^{13}C-^{13}C Aβ40	1	PCA-AD	9	0.184 (0.042)	0.222†	0.663†	37†	0.925†	14.61†	0.435†	0.670†
2D ^{13}C-^{13}C Aβ40	1	t-AD + PCA-AD	20	0.183 (0.037)	0.200†	0.579†	90†	0.618†	15.29†	0.630†	0.538†
2D ^{13}C-^{13}C Aβ40	2	RADC	8	−0.225 (0.197)							
2D ^{13}C-^{13}C Aβ40	2	t-AD	11	0.061 (0.094)	0.750*	0.637*	11*	0.004*	9.34*	−3.804*	0.004*
2D ^{13}C-^{13}C Aβ40	2	PCA-AD	9	0.131 (0.071)	0.875*	0.663*	4*	0.001*	8.613*	−4.843*	0.001*
2D ^{13}C-^{13}C Aβ40	2	t-AD + PCA-AD	20	0.093 (0.090)	0.750*	0.579*	15*	<0.001*	8.193*	−4.383*	0.002*
2D ^{13}C-^{13}C Aβ40	3	RADC	8	−0.086 (0.263)							
2D ^{13}C-^{13}C Aβ40	3	t-AD	11	0.036 (0.148)	0.409†	0.637†	34†	0.418†	10.217†	−1.183†	0.264†
2D ^{13}C-^{13}C Aβ40	3	PCA-AD	9	0.082 (0.143)	0.500†	0.663†	16†	0.053†	10.539†	−1.607†	0.138†
2D ^{13}C-^{13}C Aβ40	3	t-AD + PCA-AD	20	0.057 (0.144)	0.45†	0.579†	50†	0.129†	8.732†	−1.450†	0.182†
2D ^{15}N-^{13}C Aβ40	1	RADC	8	0.197 (0.023)							
2D ^{15}N-^{13}C Aβ40	1	t-AD	11	0.198 (0.029)	0.284†	0.637†	43†	0.936†	16.909†	−0.104†	0.918†
2D ^{15}N-^{13}C Aβ40	1	PCA-AD	6	0.199 (0.038)	0.333†	0.729†	21†	0.708†	7.621†	−0.115†	0.911†
2D ^{15}N-^{13}C Aβ40	1	t-AD + PCA-AD	17	0.199 (0.031)	0.199†	0.592†	64†	0.820†	18.784†	−0.137†	0.893†
2D ^{15}N-^{13}C Aβ40	2	RADC	8	−0.134 (0.198)							
2D ^{15}N-^{13}C Aβ40	2	t-AD	11	0.093 (0.201)	0.568†	0.637†	18*	0.029*	15.374*	−2.467*	0.026*
2D ^{15}N-^{13}C Aβ40	2	PCA-AD	6	0.070 (0.102)	0.625†	0.729†	10†	0.070†	10.911*	−2.516*	0.029*
2D ^{15}N-^{13}C Aβ40	2	t-AD + PCA-AD	17	0.085 (0.169)	0.574†	0.592†	28*	0.017*	12.013*	−2.712*	0.019*
2D ^{15}N-^{13}C Aβ40	3	RADC	8	−0.092 (0.173)							
2D ^{15}N-^{13}C Aβ40	3	t-AD	11	0.030 (0.246)	0.364†	0.637†	28†	0.191†	16.996†	−1.275†	0.219†
2D ^{15}N-^{13}C Aβ40	3	PCA-AD	6	0.028 (0.144)	0.458†	0.729†	15†	0.255†	11.812†	−1.427†	0.180†
2D ^{15}N-^{13}C Aβ40	3	t-AD + PCA-AD	17	0.030 (0.210)	0.390†	0.592†	43†	0.148†	16.617†	−1.531†	0.144†
2D ^{13}C-^{13}C Aβ42	1	RADC	8	−0.233 (0.023)							
2D ^{13}C-^{13}C Aβ42	1	t-AD	7	−0.193 (0.021)	0.857*	0.702*	5*	0.005*	12.947*	−3.511*	0.004*
2D ^{13}C-^{13}C Aβ42	1	PCA-AD	7	−0.204 (0.025)	0.607†	0.702†	10*	0.034*	12.229*	−2.296*	0.040*
2D ^{13}C-^{13}C Aβ42	1	t-AD + PCA-AD	14	−0.199 (0.023)	0.714*	0.610*	15*	0.003*	14.881*	−3.374*	0.004*
2D ^{13}C-^{13}C Aβ42	2	RADC	8	0.186 (0.130)							
2D ^{13}C-^{13}C Aβ42	2	t-AD	7	−0.197 (0.205)	0.875*	0.702*	54*	0.001*	9.933*	4.255*	0.002*
2D ^{13}C-^{13}C Aβ42	2	PCA-AD	7	−0.044 (0.106)	0.875*	0.702*	51*	0.005*	12.951*	3.766*	0.002*
2D ^{13}C-^{13}C Aβ42	2	t-AD + PCA-AD	14	−0.121 (0.176)	0.875*	0.610*	105*	<0.001*	18.408*	4.661*	<0.001*
2D ^{13}C-^{13}C Aβ42	3	RADC	8	−0.075 (0.326)							
2D ^{13}C-^{13}C Aβ42	3	t-AD	7	−0.007 (0.113)	0.375†	0.702†	27†	0.911†	8.843†	−0.547†	0.598†
2D ^{13}C-^{13}C Aβ42	3	PCA-AD	7	0.107 (0.095)	0.500†	0.702†	19†	0.308†	8.334†	−1.505†	0.169†
2D ^{13}C-^{13}C Aβ42	3	t-AD + PCA-AD	14	−0.050 (0.116)	0.375†	0.610†	46†	0.504†	8.033†	−1.043†	0.328†
2D ^{15}N-^{13}C Aβ42	1	RADC	8	−0.220 (0.017)							
2D ^{15}N-^{13}C Aβ42	1	t-AD	7	−0.241 (0.037)	0.589†	0.702†	39†	0.210†	8.241†	1.333†	0.218†
2D ^{15}N-^{13}C Aβ42	1	PCA-AD	4	−0.220 (0.028)	0.375†	0.813†	17†	0.871†	4.185†	−0.039†	0.970†
2D ^{15}N-^{13}C Aβ42	1	t-AD + PCA-AD	11	−0.233 (0.034)	0.420†	0.637†	56†	0.330†	15.512†	1.063†	0.304†
2D ^{15}N-^{13}C Aβ42	2	RADC	8	0.197 (0.067)							
2D ^{15}N-^{13}C Aβ42	2	t-AD	7	−0.185 (0.229)	1.000*	0.702*	56*	<0.001*	6.897*	4.263*	0.004*
2D ^{15}N-^{13}C Aβ42	2	PCA-AD	4	0.030 (0.180)	0.750†	0.813†	27†	0.060†	3.423†	1.801†	0.158†
2D ^{15}N-^{13}C Aβ42	2	t-AD + PCA-AD	11	−0.107 (0.230)	0.909*	0.637*	83*	<0.001*	12.225*	4.151*	0.001*
2D ^{15}N-^{13}C Aβ42	3	RADC	8	−0.070 (0.358)							
2D ^{15}N-^{13}C Aβ42	3	t-AD	7	0.047 (0.031)	0.625†	0.702†	19†	0.308†	7.121†	−0.918†	0.389†
2D ^{15}N-^{13}C Aβ42	3	PCA-AD	4	0.100 (0.027)	0.750†	0.831†	8†	0.183†	7.157†	−1.328†	0.225†
2D ^{15}N-^{13}C Aβ42	3	t-AD + PCA-AD	11	0.066 (0.039)	0.625†	0.637†	27†	0.164†	7.119†	−1.068†	0.321†

Results from WMW, KS, and WTT tests in t-AD, PCA-AD, and t-AD + PCA-AD rows represent comparisons with principal component coefficients of RADC data.

*Statistically significant differences from coefficients for RADC samples.

†An absence of statistical significance.

polymorphism are the primary determinants of cognitive status in subjects with high amyloid loads.

It has been proposed that cognitively normal subjects with high amyloid loads are in a preclinical phase of AD, meaning that they would eventually develop dementia (64). The absence of detectable cognitive impairment may be a consequence of large cognitive reserve in these individuals (65) and/or differential susceptibility to Aβ-induced neurotoxicity via variation in Aβ receptors (7). If neurodegeneration is driven largely by tau pathology that develops as a consequence of amyloid deposition (66), then variations in the strength of the Aβ-tau connection or susceptibility to tau-induced dysfunction could explain variations in cognitive impairment among individuals with high amyloid loads. The differences in relative populations of Aβ fibril polymorphs indicated by the solid-state NMR data could then conceivably be a consequence of feedback, in which a neurodegenerative state, originally induced by amyloid formation, later alters the

rates of clearance and self-propagation of certain Aβ fibril polymorphs. In this scenario, development of AD in some individuals with high amyloid loads, but not in others, would not be determined by differences in their Aβ fibril structures. However, after neurodegeneration became more pronounced in some individuals, the relative populations of various polymorphs in brain tissue of those with or without obvious cognitive impairment could become different on average.

Methods

Brain tissue extracts were prepared as previously described (21, 22). Fibrils were grown as described above and depicted in Fig. 1*A*. Solid-state NMR spectra were obtained with standard pulse sequences using magnetic field strengths of 14.1 and 17.5 T and magic-angle spinning frequencies of 13.6 and 17.0 kHz, respectively; rmsd and principal component analyses of 2D spectra were performed as previously described (22). Full details of samples, experiments, and data analyses are given in *SI Appendix*, *SI Methods*.

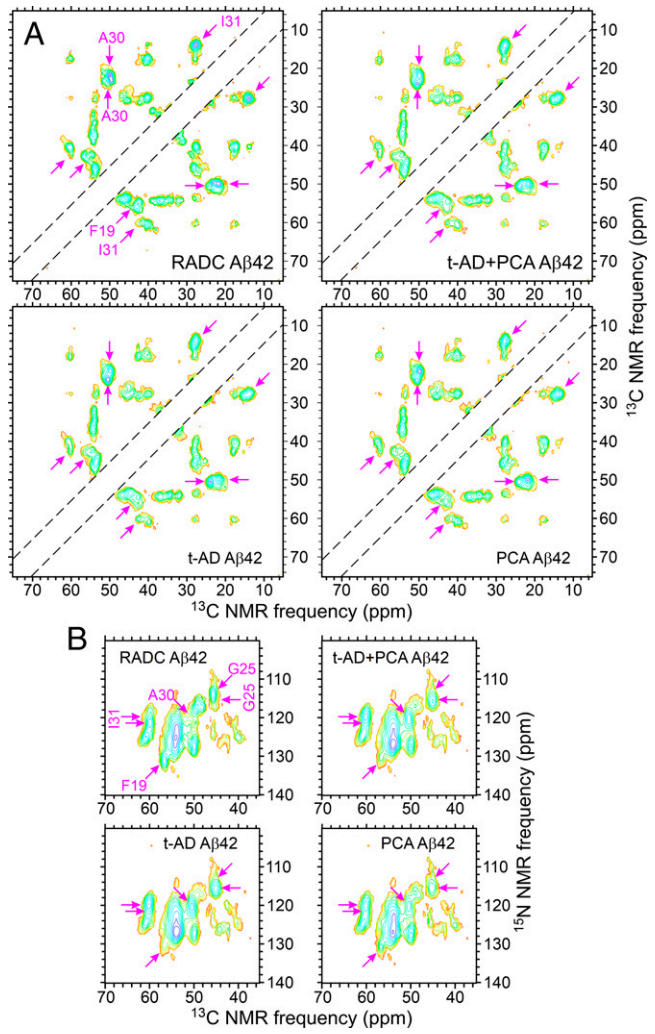

Fig. 6. Average 2D spectra generated from principal component spectra using the average coefficients of the first three principal components in each tissue category. (*A*) Average 2D ^{13}C-^{13}C spectra of isotopically labeled Aβ40 fibrils derived from RADC, t-AD, and PCA-AD tissue samples. Combined averages for t-AD and PCA-AD samples are shown as t-AD + PCA. Sixteen contour levels are shown, increasing by factors of 1.4 and with colors ranging from red to blue. Diagonal regions within dashed lines were not included in the principal component analysis. Magenta arrows indicate cross-peaks with subtle variations in relative intensities. (*B*) Same as in *A* for 2D ^{15}N-^{13}C spectra. The numbers of spectra used to calculate averages for RADC, t-AD + PCA, t-AD, and PCA-AD categories are 8, 20, 11, and 9, respectively, in *A* and 8, 17, 11, and 6, respectively, in *B*.

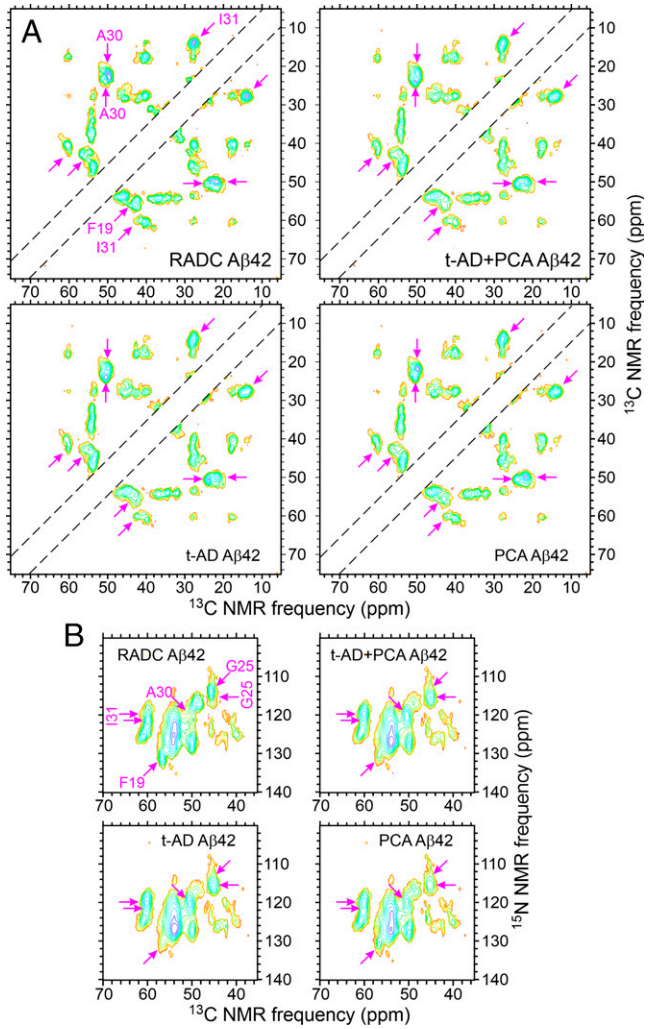

Fig. 7. Average 2D spectra of isotopically labeled Aβ42 fibrils as in Fig. 6. The numbers of spectra used to calculate averages for RADC, t-AD + PCA, t-AD, and PCA-AD categories are 8, 14, 7, and 7, respectively, in *A* and 8, 11, 7, and 4, respectively, in *B*.

Data and Code Availability. The 2D solid-state NMR spectra data that support the findings of this study have been deposited in Mendeley Data (https://data.mendeley.com/datasets/dj34fwjhkt/1). Computer programs written specifically for the analyses in Figs. 4 and 5 have been deposited in Mendeley Data (https://data.mendeley.com/datasets/3zzc2dhx26/1). Previously published data were also used for this work (https://data.mendeley.com/datasets/tbp45pm92x/1).

ACKNOWLEDGMENTS. This work was supported by the Intramural Research Program of the National Institute of Diabetes and Digestive and Kidney Diseases, NIH. The Medical Research Council (MRC) Prion Unit at University College London (UCL) is funded by the UK Medical Research Council and the National Institute of Health Research University College London Hospital/UCL Biomedical Research Centre. We thank Drs. David Bennett and Zoe Arvanitakis of RADC for providing tissue samples, with support from NIH Grants P30AG010161 and R01AG15819. We are grateful for the assistance of S. Mead, O. Avwenagha, and J. Wadsworth at the MRC Prion Unit in the selection and processing of AD tissue samples. We thank all patients and their families for consent to use tissues in research. We also thank the Queen Square Brain Bank for Neurological Disorders (supported by the Reta Lila Weston Trust for Medical Research, the Progressive Supranuclear Palsy [Europe] Association, and the MRC) at the UCL Institute of Neurology for provision of AD tissue samples.

1. D. J. Selkoe, J. Hardy, The amyloid hypothesis of Alzheimer's disease at 25 years. *EMBO Mol. Med.* **8**, 595–608 (2016).
2. R. Deane, B. V. Zlokovic, Role of the blood-brain barrier in the pathogenesis of Alzheimer's disease. *Curr. Alzheimer Res.* **4**, 191–197 (2007).
3. P. Eikelenboom *et al.*, Neuroinflammation - An early event in both the history and pathogenesis of Alzheimer's disease. *Neurodegener. Dis.* **7**, 38–41 (2010).
4. H. H. Jarosz-Griffiths, E. Noble, J. V. Rushworth, N. M. Hooper, Amyloid-β receptors: The good, the bad, and the prion protein. *J. Biol. Chem.* **291**, 3174–3183 (2016).
5. A. S. Pithadia, M. H. Lim, Metal-associated amyloid-β species in Alzheimer's disease. *Curr. Opin. Chem. Biol.* **16**, 67–73 (2012).
6. D. A. Delgado *et al.*, Distinct membrane disruption pathways are induced by 40-residue β-amyloid peptides. *J. Biol. Chem.* **291**, 12233–12244 (2016).
7. S. A. Purro, A. J. Nicoll, J. Collinge, Prion protein as a toxic acceptor of amyloid-β oligomers. *Biol. Psychiatry* **83**, 358–368 (2018).
8. P. Giannakopoulos, P. R. Hof, J. P. Michel, J. Guimon, C. Bouras, Cerebral cortex pathology in aging and Alzheimer's disease: A quantitative survey of large hospital-based geriatric and psychiatric cohorts. *Brain Res. Brain Res. Rev.* **25**, 217–245 (1997).
9. G. M. Savva *et al.*, Medical Research Council Cognitive Function and Ageing Study, Age, neuropathology, and dementia. *N. Engl. J. Med.* **360**, 2302–2309 (2009).
10. H. J. Aizenstein *et al.*, Frequent amyloid deposition without significant cognitive impairment among the elderly. *Arch. Neurol.* **65**, 1509–1517 (2008).
11. C. A. Mathis *et al.*, In vivo assessment of amyloid-β deposition in nondemented very elderly subjects. *Ann. Neurol.* **73**, 751–761 (2013).
12. M. J. Grothe, M. Ewers, B. Krause, H. Heinsen, S. J. Teipel; Alzheimer's Disease Neuroimaging Initiative, Basal forebrain atrophy and cortical amyloid deposition in nondemented elderly subjects. *Alzheimers Dement.* **10**, S344–S353 (2014).
13. Y. Gu *et al.*, Brain amyloid deposition and longitudinal cognitive decline in nondemented older subjects: Results from a multi-ethnic population. *PLoS One* **10**, e0123743 (2015).
14. B. J. Cummings, C. J. Pike, R. Shankle, C. W. Cotman, β-amyloid deposition and other measures of neuropathology predict cognitive status in Alzheimer's disease. *Neurobiol. Aging* **17**, 921–933 (1996).
15. J. Näslund *et al.*, Correlation between elevated levels of amyloid β-peptide in the brain and cognitive decline. *JAMA* **283**, 1571–1577 (2000).
16. V. L. Villemagne *et al.*, Abeta deposits in older non-demented individuals with cognitive decline are indicative of preclinical Alzheimer's disease. *Neuropsychologia* **46**, 1688–1697 (2008).
17. C. R. Jack, Jr *et al.*, Alzheimer's Disease Neuroimaging Initiative, Serial PIB and MRI in normal, mild cognitive impairment and Alzheimer's disease: Implications for sequence of pathological events in Alzheimer's disease. *Brain* **132**, 1355–1365 (2009).
18. C. Goldsbury, P. Frey, V. Olivieri, U. Aebi, S. A. Müller, Multiple assembly pathways underlie amyloid-β fibril polymorphisms. *J. Mol. Biol.* **352**, 282–298 (2005).
19. A. T. Petkova *et al.*, Self-propagating, molecular-level polymorphism in Alzheimer's β-amyloid fibrils. *Science* **307**, 262–265 (2005).
20. R. Tycko, Amyloid polymorphism: Structural basis and neurobiological relevance. *Neuron* **86**, 632–645 (2015).
21. J. X. Lu *et al.*, Molecular structure of β-amyloid fibrils in Alzheimer's disease brain tissue. *Cell* **154**, 1257–1268 (2013).
22. W. Qiang, W. M. Yau, J. X. Lu, J. Collinge, R. Tycko, Structural variation in amyloid-β fibrils from Alzheimer's disease clinical subtypes. *Nature* **541**, 217–221 (2017).
23. M. Kollmer *et al.*, Cryo-EM structure and polymorphism of Aβ amyloid fibrils purified from Alzheimer's brain tissue. *Nat. Commun.* **10**, 1–8 (2019).
24. U. Ghosh, K. R. Thurber, W. M. Yau, R. Tycko, Molecular structure of a prevalent amyloid-β fibril polymorph from Alzheimer's disease brain tissue. *Proc. Natl. Acad. Sci. U.S.A.* **118**, e2023089118 (2021).
25. Y. Xiao *et al.*, Aβ(1-42) fibril structure illuminates self-recognition and replication of amyloid in Alzheimer's disease. *Nat. Struct. Mol. Biol.* **22**, 499–505 (2015).
26. M. A. Wälti *et al.*, Atomic-resolution structure of a disease-relevant Aβ(1-42) amyloid fibril. *Proc. Natl. Acad. Sci. U.S.A.* **113**, E4976–E4984 (2016).
27. L. Gremer *et al.*, Fibril structure of amyloid-β(1-42) by cryo-electron microscopy. *Science* **358**, 116–119 (2017).
28. H. S. Wang *et al.*, Polymorphic Aβ42 fibrils adopt similar secondary structure but differ in cross-strand side chain stacking interactions within the same β-sheet. *Sci. Rep.* **10**, 1–9 (2020).
29. M. T. Colvin *et al.*, Atomic resolution structure of monomorphic Aβ(42) amyloid fibrils. *J. Am. Chem. Soc.* **138**, 9663–9674 (2016).
30. J. Collinge, Mammalian prions and their wider relevance in neurodegenerative diseases. *Nature* **539**, 217–226 (2016).
31. B. Caughey, G. J. Raymond, R. A. Bessen, Strain-dependent differences in β-sheet conformations of abnormal prion protein. *J. Biol. Chem.* **273**, 32230–32235 (1998).
32. J. Safar *et al.*, Eight prion strains have $PrP^{(Sc)}$ molecules with different conformations. *Nat. Med.* **4**, 1157–1165 (1998).
33. D. W. Sanders *et al.*, Distinct tau prion strains propagate in cells and mice and define different tauopathies. *Neuron* **82**, 1271–1288 (2014).
34. B. Falcon *et al.*, Structures of filaments from Pick's disease reveal a novel tau protein fold. *Nature* **561**, 137–140 (2018).
35. B. Falcon *et al.*, Novel tau filament fold in chronic traumatic encephalopathy encloses hydrophobic molecules. *Nature* **568**, 420–423 (2019).
36. A. W. P. Fitzpatrick *et al.*, Cryo-EM structures of tau filaments from Alzheimer's disease. *Nature* **547**, 185–190 (2017).
37. W. Zhang *et al.*, Novel tau filament fold in corticobasal degeneration. *Nature* **580**, 283–287 (2020).
38. M. D. Tuttle *et al.*, Solid-state NMR structure of a pathogenic fibril of full-length human α-synuclein. *Nat. Struct. Mol. Biol.* **23**, 409–415 (2016).
39. B. Li *et al.*, Cryo-EM of full-length α-synuclein reveals fibril polymorphs with a common structural kernel. *Nat. Commun.* **9**, 1–10 (2018).
40. M. Schweighauser *et al.*, Structures of α-synuclein filaments from multiple system atrophy. *Nature* **585**, 464–469 (2020).
41. J. L. Guo *et al.*, Distinct α-synuclein strains differentially promote tau inclusions in neurons. *Cell* **154**, 103–117 (2013).
42. L. Bousset *et al.*, Structural and functional characterization of two α-synuclein strains. *Nat. Commun.* **4**, 1–13 (2013).
43. A. L. Woerman *et al.*, Familial Parkinson's point mutation abolishes multiple system atrophy prion replication. *Proc. Natl. Acad. Sci. U.S.A.* **115**, 409–414 (2018).
44. M. Meyer-Luehmann *et al.*, Exogenous induction of cerebral β-amyloidogenesis is governed by agent and host. *Science* **313**, 1781–1784 (2006).
45. J. C. Watts *et al.*, Serial propagation of distinct strains of Aβ prions from Alzheimer's disease patients. *Proc. Natl. Acad. Sci. U.S.A.* **111**, 10323–10328 (2014).
46. J. Stöhr *et al.*, Distinct synthetic Aβ prion strains producing different amyloid deposits in bigenic mice. *Proc. Natl. Acad. Sci. U.S.A.* **111**, 10329–10334 (2014).
47. M. Cohen *et al.*, Distinct strains of Aβ prions implicated in rapidly progressive Alzheimer disease. *Prion* **9**, S76–S77 (2015).
48. J. Rasmussen *et al.*, Amyloid polymorphisms constitute distinct clouds of conformational variants in different etiological subtypes of Alzheimer's disease. *Proc. Natl. Acad. Sci. U.S.A.* **114**, 13018–13023 (2017).
49. C. Condello *et al.*, Structural heterogeneity and intersubject variability of Aβ in familial and sporadic Alzheimer's disease. *Proc. Natl. Acad. Sci. U.S.A.* **115**, E782–E791 (2018).
50. D. T. Murray *et al.*, Structure of FUS protein fibrils and its relevance to self-assembly and phase separation of low-complexity domains. *Cell* **171**, 615–627.e16 (2017).
51. M. R. Elkins *et al.*, Structural polymorphism of Alzheimer's β-amyloid fibrils as controlled by an E22 switch: A solid state NMR study. *J. Am. Chem. Soc.* **138**, 9840–9852 (2016).
52. A. K. Paravastu, I. Qahwash, R. D. Leapman, S. C. Meredith, R. Tycko, Seeded growth of β-amyloid fibrils from Alzheimer's brain-derived fibrils produces a distinct fibril structure. *Proc. Natl. Acad. Sci. U.S.A.* **106**, 7443–7448 (2009).
53. U. Ghosh, W. M. Yau, R. Tycko, Coexisting order and disorder within a common 40-residue amyloid-β fibril structure in Alzheimer's disease brain tissue. *Chem. Commun. (Camb.)* **54**, 5070–5073 (2018).
54. K. D. Kloepper, W. S. Woods, K. A. Winter, J. M. George, C. M. Rienstra, Preparation of α-synuclein fibrils for solid-state NMR: Expression, purification, and incubation of wild-type and mutant forms. *Protein Expr. Purif.* **48**, 112–117 (2006).
55. S. Luca, W. M. Yau, R. Leapman, R. Tycko, Peptide conformation and supramolecular organization in amylin fibrils: Constraints from solid-state NMR. *Biochemistry* **46**, 13505–13522 (2007).
56. D. A. Bennett *et al.*, Religious orders study and Rush memory and aging project. *J. Alzheimers Dis.* **64**, S161–S189 (2018).
57. W. Qiang, W. M. Yau, R. Tycko, Structural evolution of Iowa mutant β-amyloid fibrils from polymorphic to homogeneous states under repeated seeded growth. *J. Am. Chem. Soc.* **133**, 4018–4029 (2011).
58. R. Tycko, Computer programs for RMSD and principal component analyses of 2D solid state NMR spectra. Mendeley Data. https://data.mendeley.com/datasets/3zzc2dhx26/1. Deposited 1 June 2021.
59. R. Tycko, 2D solid state NMR spectra of brain-seeded amyloid-beta fibrils. Mendeley Data. https://data.mendeley.com/datasets/dj34fwjhkt/1. Deposited 25 May 2021.
60. R. Tycko, Solid state NMR spectra of brain-seeded Abeta40 and Abeta42 fibrils. Mendeley Data. https://data.mendeley.com/datasets/tbp45pm92x/1. Deposited 4 August 2016.
61. S. Wold, K. Esbensen, P. Geladi, Principal component analysis. *Chemom. Intell. Lab. Syst.* **2**, 37–52 (1987).
62. E. R. Henry, J. Hofrichter, Singular value decomposition: Application to analysis of experimental data. *Methods Enzymol.* **210**, 129–192 (1992).
63. W. M. Yau, R. Tycko, Depletion of amyloid-β peptides from solution by sequestration within fibril-seeded hydrogels. *Protein Sci.* **27**, 1218–1230 (2018).
64. P. S. Aisen *et al.*, On the path to 2025: Understanding the Alzheimer's disease continuum. *Alzheimers Res. Ther.* **9**, 1–10 (2017).
65. D. Barulli, Y. Stern, Efficiency, capacity, compensation, maintenance, plasticity: Emerging concepts in cognitive reserve. *Trends Cogn. Sci.* **17**, 502–509 (2013).
66. M. A. Busche, B. T. Hyman, Synergy between amyloid-β and tau in Alzheimer's disease. *Nat. Neurosci.* **23**, 1183–1193 (2020).